

Diverse protostellar evolutionary states in the young cluster AFGL961

Jonathan P. Williams¹, Rita K. Mann¹, Christopher N. Beaumont¹, Jonathan J. Swift¹,
Joseph D. Adams², Joe Hora³, Marc Kassis⁴, Elizabeth A. Lada⁵, Carlos G.
Román-Zúñiga⁶

¹ *Institute for Astronomy, University of Hawaii, 2680 Woodlawn Drive, Honolulu, HI
96822; jpw@ifh.hawaii.edu*

² *Cornell University, Department of Radiophysics Space Research, Ithaca NY 14853*

³ *Harvard-Smithsonian, CfA, 60 Garden St., MS 65, Cambridge, MA 02138*

⁴ *Keck Observatory 65-1120 Mamalahoa Hwy, Kamuela, HI 96743*

⁵ *Department of Astronomy, University of Florida, Gainesville, FL 32611*

⁶ *Centro Astronómico Hispano Alemán, Camino Bajo de Huétor 50, Granada 18008, Spain*

ABSTRACT

We present arcsecond resolution mid-infrared and millimeter observations of the center of the young stellar cluster AFGL961 in the Rosette molecular cloud. Within 0.2 pc of each other, we find an early B star embedded in a dense core, a neighboring star of similar luminosity with no millimeter counterpart, a protostar that has cleared out a cavity in the circumcluster envelope, and two massive, dense cores with no infrared counterparts. An outflow emanates from one of these cores, indicating a deeply embedded protostar, but the other is starless, bound, and appears to be collapsing. The diversity of states implies either that protostellar evolution is faster in clusters than in isolation or that clusters form via quasi-static rather than dynamic collapse. The existence of a pre-stellar core at the cluster center shows that that some star formation continues after and in close proximity to massive, ionizing stars.

Subject headings: circumstellar matter – stars: formation — stars: pre-main sequence — ISM: structure

1. Introduction

The dominant mode of star formation is in groups. In this sense, understanding cluster formation is a prerequisite for understanding the origin of most stars, including all massive stars and, in all likelihood, our Sun. Some major unanswered questions include the role of global and local processes, the formation time-scale, and whether high mass stars shut down further cluster growth.

Long wavelength, mid-infrared to millimeter, observations are required to image the youngest, most deeply embedded protostars and their nascent cores. The study of dense stellar groups is hampered by the low resolution at these wavelengths and, consequently, less is known about their origins and evolution than closer, isolated star forming systems. Technological developments including large format mid-infrared arrays and sensitive millimeter interferometers provide a new view of the most embedded regions of young clusters. We report here observations of young protostars and molecular cores in the AFGL961 cluster and the constraints that these place on models of cluster formation.

AFGL961 owes its name to an Air Force infrared sky survey carried out on a rocket-borne telescope in the early 1970s. The resolution of these data was low and Cohen (1973) was the first to give a precise, ground-based, position. Due to its high luminosity and location in the nearby Rosette molecular cloud, AFGL961 has been the subject of many subsequent studies.

Bally & Predmore (1983) found a weak point-like 5 GHz source with the VLA and interpreted it as a compact HII region around a B3 star. Based on the definition of Zinnecker & Yorke (2007), AFGL961 can therefore be considered as a (borderline) massive star forming region. Near-infrared imaging by Lenzen et al. (1984) revealed a double source with the easternmost, redder component coinciding with the VLA source. They also found a third object about 30" further west near the most prominent optical emission, a fan-shaped reflection nebula. Castelaz et al. (1985) confirmed the double source and showed that both members are pre-main-sequence with the luminosity of B stars. Aspin (1998) presented a wide field image of shocked H₂ emission showing numerous stellar sources and bow shock structures. Román-Zúñiga et al. (2008) mapped the entire Rosette molecular cloud in the near-infrared and identified 10 embedded clusters of which AFGL961 is the brightest and the most heavily obscured by nebulosity. This obscuration, however, prevented a detailed study of the fainter and most embedded sources.

AFGL961 lies in a massive clump along a broad ridge of molecular emission extending away from the Rosette nebula (Blitz & Thaddeus 1980). Lada & Gautier (1982) mapped a bipolar outflow from the cluster, most recently imaged in CO 3–2 by Dent et al. (2009) who show a high velocity, collimated flow extending over 5'.

Distance estimates to the Rosette cloud range from 1.4 – 1.7 kpc (Ogura & Ishida 1981; Perez et al. 1987; Hensberge et al. 2000) and we adopt 1.6 kpc here for consistency with most previous work. AFGL961 has an infrared luminosity of $11400 L_{\odot}$ (Cox et al. 1990) and is, by far, the brightest embedded cluster in the cloud.

A large-scale view of AFGL961 is shown in Figure 1. The image is from the observations of Román-Zúñiga et al. (2008) and shows the embedded protostars and associated nebulosity at $2.2 \mu\text{m}$. The contours show the emission at $850 \mu\text{m}$ from the dusty cluster envelope and were produced from archival SCUBA data. The flux per beam at this wavelength is a direct measure of column density where we have assumed a uniform temperature $T = 20 \text{ K}$ and dust opacity $\kappa_{\nu} = 0.1(\nu/1200 \text{ GHz}) \text{ cm}^2 \text{ g}^{-1}$ (Hildebrand 1983). The contours are in units of g cm^{-2} to best compare to theoretical calculations and numerical simulations (see §4). The total flux of the map is 10 Jy which converts to a mass $M = 90 M_{\odot}$. Three bright stars dominate the luminosity of the cluster at this wavelength and through the mid-infrared (Poulton et al. 2008). The dust peak is slightly elongated and offset from the central double source and the western source at the center of the optical fan-shaped nebulosity lies near the edge of the envelope.

We have gathered data on AFGL961 over a period of several years with the Infrared Telescope Facility¹ (IRTF), Submillimeter Array² (SMA), and James Clerk Maxwell Telescope³ (JCMT) at the Mauna Kea Observatory. Our observations, detailed in §2, are centered on the white box in Figure 1. The data, presented in §3, reveal a surprising diversity of evolutionary states at the cluster center, including the discovery of a Class 0 and starless core neighboring the known infrared sources. We discuss the implications of this work for understanding cluster formation in §4 and conclude in §5.

¹ The Infrared Telescope Facility, is operated by the University of Hawaii under Cooperative Agreement no. NCC 5-538 with the National Aeronautics and Space Administration, Science Mission Directorate, Planetary Astronomy Program.

² The Submillimeter Array is a joint project between the Smithsonian Astrophysical Observatory and the Academia Sinica Institute of Astronomy and Astrophysics and is funded by the Smithsonian Institution and the Academia Sinica.

³ The James Clerk Maxwell Telescope is operated by The Joint Astronomy Centre on behalf of the Science and Technology Facilities Council of the United Kingdom, the Netherlands Organisation for Scientific Research, and the National Research Council of Canada.

2. Observations

We used the MIRSI camera on the IRTF (Kassis et al. 2008) to map the mid-infrared emission on December 12th 2003. Images were taken in the M, N, and Q filters centered at 4.9, 10.4, and 20.9 μm respectively using a $5'' \times 5''$ dither. The skies were clear, cold and dry, and images were diffraction limited at $0''.5$, $0''.9$, and $1''.7$ respectively. Sky subtraction was obtained by chopping $30''$ North-South and nodding $40''$ East-West. This kept the cluster on the array at all times and maximized the sensitivity in the registered and co-added maps. Calibration was performed by observations of α Canis Minor (Procyon) bracketing the AFGL961 observations. The final maps were made using an IDL reduction pipeline written by support astronomer E. Volquardsen. Three sources were detected (Figure 2) and all have counterparts in the 2MASS catalog. We therefore used the latter to define the astrometry.

The SMA observations were carried out under dry and stable skies on 13th December 2005 in the compact configuration (20–70 m baselines) and in a partial track on 4th February 2006 in the extended configuration (70 – 240 m baselines). A mosaic of two Nyquist-spaced pointings was made to ensure approximately uniform coverage over the MIRSI field. The receiver was tuned to place the $\text{H}_2\text{CO } 3_{12} - 2_{11}$ line at 225.7 GHz in the upper sideband and DCN 3–2 at 217.2 GHz in the lower sideband with a resolution of 0.81 MHz (1.1 km s^{-1}) per channel. The time dependence of the gains was measured via observations of 0530+135 interleaved with the source, the shape of the passband was measured by deep observations of 3C454.3 and 3C111, and observations of Uranus were used to set the flux scale. The visibilities were calibrated with the MIR software package and maps were then produced using standard MIRIAD routines. A continuum image centered at $1400 \mu\text{m}$ was produced by combining the 2 GHz lower and upper sidebands from the compact and extended configuration datasets and inverting with natural weighting. The resulting resolution and noise is $3''.1 \times 2''.8$ and 3 mJy beam^{-1} . We also produced a higher resolution map, $1''.4 \times 0''.9$, at the expense of increased noise, by inverting with higher weights on the longer baselines. In this paper, we use the former to measure the distribution and masses of the cores, and the latter to measure core locations and determine their association (or lack thereof) with mid-infrared sources. The lines were undetected on the long baselines and maps were made using the compact configuration data only using natural weighting. The resolution and noise in the H_2CO map are $3''.7 \times 3''.4$ and 0.17 K. The corresponding numbers for the DCN map are $3''.8 \times 3''.6$ and 0.08 K.

As interferometers are unable to measure the flux at small spatial frequencies, we used Receiver A on the JCMT to observe the same H_2CO line as the SMA observations. We mapped a $3' \times 3'$ region centered on the peak of the SMA map on 19th March 2008. The

map was made using the on-the-fly mapping mode with a nearby reference position that was first verified to be free of emission. Data reduction was carried out with the STARLINK package. The JCMT map and SMA dirty map were weighted by their respective beam areas, combined in the image plane, and cleaned with a similarly combined beam following the method detailed in Stanimirovic (2002). The resulting map retains the high resolution in the interferometer map and, as the signal-to-noise ratio was very high in the JCMT data, the noise is similar, 0.17 K per channel, as the SMA data.

3. Results

3.1. Morphology

The MIRSI maps are shown in Figure 2. The three infrared sources first seen by Lenzen et al. (1984) are detected in each filter. To avoid confusion, particularly for the varied “western” nomenclature, we label them AFGL961A, B and C in order of infrared luminosity. The positions and fluxes of each source are listed in Table 1. The fluxes of each source sharply rise with wavelength indicating that they are deeply embedded. The infrared spectral energy distributions (SEDs) are discussed in more detail in §4; we focus here on the morphological differences. AFGL961C is slightly elongated in the N-band image and the emission at Q-band is very extended. Aspin (1998) found H₂ bow shock features on either side of the star and Li et al. (2008) present a detailed study of these features. The position angle of the elongated structure in the Q-band image lines up with these and the extended mid-infrared emission is likely to be from hot dust filling a cavity that the star has blown out around itself.

The differences between the sources are even more striking at 1400 μm . Figure 3 shows the SMA continuum map in relation to the infrared sources. As for the SCUBA map in Figure 1, the contour units are converted from flux per beam to a mass surface density assuming $T = 20$ K and a Hildebrand (1983) dust opacity, $\kappa = 0.018 \text{ cm}^2 \text{ g}^{-1}$. Three prominent sources, strung out along a filament, are detected and labeled SMA1–3. Their positions and fluxes are listed in Table 2. There is a negligible $0''.2$ offset between the peak of the SMA1 core and AFGL961A. The $1''.6$ offset between SMA2 and AFGL961B is significant, however. A closeup of the region with the higher resolution continuum map is discussed in §3.2 and more clearly shows the distinction between these two objects.

We therefore consider SMA1 to be the dusty envelope around the pre-main-sequence B star AFGL961A and suggest that SMA2 is a distinct source in the cluster, a dense core that lacks an infrared counterpart at the limits of detection in the MIRSI map. SMA3 is the brightest source in the 1400 μm map and also lacks an infrared counterpart. Both

these sources are also undetected in 2MASS images and the deeper JHK observations of Román-Zúñiga et al. (2008).

The MIRSI data show that any embedded object in SMA2 or SMA3 is more than 500 times fainter than AFGL961A from 4.9-20.9 μm but this does not rule out a solar mass protostar. For the case of the relatively isolated SMA3 core, we can place far more stringent limits on the infrared luminosity from the Spitzer observations of Poulton et al. (2008). We plot the SMA continuum map in contours over the IRAC 3.6 μm image in the lower panel of Figure 3. No infrared source is apparent at the position of SMA3 in this image or in the other IRAC bands. Comparing with faint stars in the cluster and taking into account the point spread function and extended nebulosity, we estimate the limits on the flux of any embedded object in SMA3 to be 0.4, 0.8, 1.2, and 2 mJy at 3.6, 4.5, 5.8, and 8.0 μm respectively. Many of the low mass, moderately embedded protostars in Perseus (Jørgensen et al. 2006) would have been detected at this level. SMA2 is lost in the glare around AFGL961A,B of the IRAC images so these limits do not apply in that case.

The Q-band data are critical for ruling out very deeply embedded protostars. Based on the SED models of Robitaille et al. (2006), we estimate that the most luminous object consistent with our MIRSI upper limits in SMA2 and SMA3 is a $300 L_{\odot}$ protostar behind $\gtrsim 100$ magnitudes of visual extinction. Unfortunately the Spitzer MIPS 24 μm image is heavily saturated and the SMA2 and SMA3 cores lie in the point spread function wings of AFGL961A,B. de Wit et al. (2009) recently imaged the AFGL961A,B pair at 24.5 μm with the 8 m Subaru telescope. Their map also shows no source within SMA2 but the field-of-view is too small to include SMA3. The resolution of these data is higher than our MIRSI Q-band image but the sensitivity does not appear to be significantly greater.

At the other extreme of the MIRSI-SMA comparison, the bright infrared source AFGL961C is not detected in the 1400 μm map. This indicates a lack of compact, cool dust around it and, despite the similarities of the mid-infrared spectral slopes, places it at a more advanced evolutionary state than AFGL961A which is fully embedded in a cold molecular core.

The millimeter fluxes can be converted directly to a mass assuming a temperature and dust grain opacity. Masses are listed in Table 2 under the same prescription for the envelope mass calculation in §1. The three cores have similar fluxes and, hence, similar inferred masses. However, we might expect SMA1, which contains a B star, to be hotter than SMA2 and 3 and its mass to be proportionately lower than listed here.

The principal finding from our examination of the IRTF and SMA maps is the detection of 5 distinct pre- or proto-stellar sources within the central regions of the cluster. AFGL961 A is embedded in a dense core, AFGL961 B and C lack a similarly sized cold dusty envelope, and there are two moderately massive cores, SMA2 and 3 that lack bright infrared sources.

3.2. Dynamics

Our SMA data provide spectroscopic information at $\sim 1 \text{ km s}^{-1}$ resolution and allow us to study the dynamics of the dusty cores detected in the continuum. We chose a tuning that placed 3–2 rotational transitions of H_2CO in the upper sideband and DCN in the lower sideband. The former molecule is abundant in protostellar envelopes and a good tracer of infall motions (Mardones et al. 1997), the latter, as a deuterated species, is well suited for pinpointing the cold, potentially pre-stellar gas (Stark et al. 1999) and measuring the systemic motions of the core. Figure 4 shows the integrated intensity of $\text{H}_2\text{CO } 3_{12} - 2_{11}$ and DCN 3–2 overlaid on the continuum. Both lines follow the same filamentary structure as the dust. The H_2CO map shows a very strong peak toward SMA2 and a weaker peak toward SMA3. The small offsets between the line and dust peaks is likely due to the high opacity of this line. The DCN emission is weaker but more closely follows the dust morphology. There is a single peak toward SMA2 but enhanced emission toward SMA1 and 3 is also evident.

The close correspondence between the DCN and continuum maps shows that we can use the former to estimate the velocity dispersion, σ , of the SMA1–3 cores. The central velocities, linewidths, $\Delta v = 2.355\sigma$, and virial masses, $M_{\text{vir}} = 3R\sigma^2/G$, are listed in Table 2. The latter assumes spherical cores with an inverse square density profile (Bertoldi & McKee 1992). At the resolution of these data, it is hard to determine with much certainty where the cores end and the filament begins from the continuum map in Figure 3 but, depending on the intensity threshold used to define their limits, we estimate core radii $\sim 3 - 4''$ from their projected area indicating that the cores are barely resolved with deconvolved sizes $\lesssim 5000 \text{ AU}$. We find that the virial masses of SMA1 and 3 exceed the measured masses by about a factor of two indicating an approximate balance between kinetic and potential energy in these two cores. The large virial mass of SMA2, due its high linewidth, indicates that this core is unbound.

The intense H_2CO emission toward SMA2 is likely due to grain mantle sputtering or evaporation and signposts an embedded protostar. Indeed, inspection of the spectra and channel maps reveal an outflow centered on this core with line wings discernible from $4 - 22 \text{ km s}^{-1}$. Figure 5 zooms in on this region and shows the most intense emission from the blue and redshifted sides of the line. The two moment maps are offset from each other and on opposite sides of the continuum emission. The discovery of this outflow explains the high DCN linewidth, why the core is unbound, and confirms that SMA2 is a physically distinct object from AFGL961B.

SMA3 also lacks a detectable infrared source but has a much smaller linewidth and appears to be bound. The H_2CO data does not show any evidence for an outflow but the spectrum toward the core is asymmetric and shows a small dip at the velocity of the DCN

line (Figure 6). This is indicative of red-shifted self-absorption and a signature of infall motion. Unfortunately the velocity resolution of these data is poor and the self-absorption is seen in only one spectra channel. We were consequently unable to successfully fit the spectra using the radiative transfer models of De Vries & Myers (2005). As there is some ambiguity in modeling the interferometric data alone without knowledge of the larger scale emission, we observed the same line with the JCMT and made a fully sampled H₂CO datacube. The integrated intensity is shown as dotted contours in Figure 4. The combined JCMT+SMA map show the large scale cluster envelope emission, similar to the SCUBA map in Figure 1 and the individual pre- and proto-stellar cores are not apparent. No self-absorption is seen in the combined spectra across the cluster and toward SMA3 in particular. Hence there is no evidence from these data for large scale collapse onto the cluster.

4. Discussion

4.1. Evolutionary states

Our IRTF images from 5 – 20 μm show the most deeply embedded, luminous stars in the cluster. The sensitivity of these images is much lower than the Spitzer data but the resolution is higher and the fidelity of the bright sources better. We do not find any new sources that are not seen in existing near-infrared images but we show that the three known members, AFGL961A, B, and C, each have rising spectral indices in the mid-infrared. The SEDs are plotted in Figure 7. We have fit the near- and mid-infrared data using the precomputed models of Robitaille et al. (2006, 2007). As the model SEDs are noisy at millimeter wavelengths we have not fit the SMA data point but show the interpolation between model and 1400 μm flux. The model parameters include a central source, disk, and envelope. In each case, most fits show the sources are embedded under more than 20 magnitudes of extinction. The precise amount is not well constrained (although background sources are ruled out). Similarly, a wide range of disk and envelope parameters can fit the data and their masses are not well determined. However, all the fits show that the envelope dominates, typically by more than a factor of 100. The best constrained parameters are the total luminosity and stellar mass of the source. These are tabulated in Table 3 for the best fit and the mean and standard deviation of the top 100 fits, weighted by the inverse of χ^2 . The three sources are all massive stars but the morphological differences and comparison with the millimeter map shows that they are in quite different evolutionary states.

AFGL961A,B have been considered a binary system based on their close proximity to each other (e.g. Aspin 1998). However, their properties at 1400 μm are quite different: source A is embedded in the dense 6 M_{\odot} SMA1 core but there is no millimeter emission centered on

source B. Using the higher resolution continuum map (Figure 5) we can place a 3σ limit on the $1400\ \mu\text{m}$ flux toward source B of 9 mJy ($0.3 M_\odot$) at ~ 2000 AU scales. AFGL961A,B did not form from a common core, therefore, and are not a binary pair but simply neighboring protostars, in different evolutionary states, in a dense cluster.

AFGL961C is different in its own way. It is a point source in the M-band image, noticeably elongated at N-band, and a large cavity of hot dust is seen in the Q-band image. This star is clearing out its surrounding material, as also shown by the shocked H_2 emission image of Aspin (1998). Li et al. (2008) postulated that the hourglass shape of the infrared nebula is due to polar winds from a very young protostar punching a hole in its surrounding core. No core emission is detected at $1400\ \mu\text{m}$, however, and the same $0.3 M_\odot$ limit at ~ 2000 AU scales applies as for source B.

The ratio of stellar to envelope mass, M_*/M_{env} , is an effective measure of protostellar evolutionary state (Andre et al. 1993). There is certainly some uncertainty in determining each of these quantities but it is clear that there is a large range in the ratio. $M_*/M_{\text{env}} \approx 2$ for AFGL961A but is greater than 30 for AFGL961B and greater than 15 for AFGL961C.

The outflow toward SMA2 indicates an embedded protostar and the non-detection in the infrared limit the bolometric luminosity to less than $300 L_\odot$. Depending on its age, this constrains the stellar mass to no more than $6 M_\odot$ and probably much lower (Siess et al. 2000). Therefore $M_*/M_{\text{env}} \lesssim 1$ and this is a Class 0 object. Given its youth and the bipolar H_2CO structure we see toward it, we further suggest that this source is the driving source of the energetic CO outflow from the cluster (Lada & Gautier 1982; Dent et al. 2009) and not the more luminous infrared sources.

SMA3 is far enough offset from the bright cluster center for the Spitzer/IRAC data to provide the most stringent limits on any embedded object and it appears to be truly starless. As it is gravitationally bound and very dense with a free-fall time, $t_{\text{ff}} \sim 10^4$ yr, it is likely to be on the brink of star formation. The interferometric H_2CO spectrum shows evidence that the core is collapsing but higher spectral resolution data are required to confirm this, and to allow modeling and a determination of the infall speed. The difference between the peak and self-absorption dip is an approximate measure and suggests $v_{\text{in}} \sim 1\ \text{km s}^{-1}$. Adding in the short spacing information from the JCMT swamps the self-absorption showing that any inward motions are on small scales. That is, the core is collapsing on itself rather than growing through the accretion of envelope material. With a mass of $6 M_\odot$, SMA3 is more massive than starless cores in isolated star forming regions such as Taurus (Shirley et al. 2000). Presumably it will form a correspondingly more massive star but probably not comparable to AFGL961A.

A mix of early evolutionary states in clusters is not uncommon. The first core identified

as a Class 0 object, VLA1623 in ρ Ophiuchus, sits on the edge of a small group of pre-stellar cores (Andre et al. 1993). Williams & Myers (1999) found a collapsing starless core adjacent to a Class I protostar in the Serpens cluster and Swift & Welch (2008) found a range of young stellar objects, from Class 0 to III, in L1551. These are all low mass objects in low mass star forming regions. Radio observations of the W3 and W75N massive star forming regions show a range of HII region morphologies and spectral indices indicating different evolutionary states (Tieftrunk et al. 1997; Shepherd et al. 2004, respectively). In particular, Shepherd et al. (2004) were able to estimate an age spread of at least 1 Myr between a cluster of five early B stars based on Strömberg sphere expansion. The detection of cold, dense pre-stellar cores and young lower mass protostars require observations at millimeter wavelengths. Interferometer maps by Hunter et al. (2006) and Rodón et al. (2008) show tight groups of dusty cores in NGC6334I and W3IRS5 respectively. Core separations are even smaller and masses higher than we have found here in the lower luminosity AFGL961 cluster. The cores have a range of infrared properties and some power outflows and they likely span a range of evolutionary states. There does not appear, however, to be a clear counterpart to the pre-stellar core, AFGL961-SMA3, with its combination of low limit to the luminosity of any embedded source and lack of outflow.

4.2. Dynamic or equilibrium cluster formation?

Theoretical models of cluster formation divide into two camps: a global collapse of a massive molecular clump or piecemeal growth from the formation of individual protostars in a more local process. The former occurs on short, dynamical time-scales (Bate et al. 2003) but the latter is more gradual and the cluster forming clump is in quasi-equilibrium (Tan et al. 2006).

Based on the SCUBA image in Figure 1, the cluster envelope has a mass $M \approx 90 M_{\odot}$ within a radius $R \approx 0.25$ pc. The free-fall timescale for this region, based on the inferred average density, $\rho \approx 10^{-19} \text{ g cm}^{-3}$, is $t_{\text{ff}} = (3\pi/32G\rho)^{1/2} \approx 0.2$ Myr. Note that material on larger scales, for example in the surrounding CO clump (Williams et al. 1995), would have a longer collapse timescale.

Our observations of a filamentary structure at high surface densities, $\Sigma \approx 0.1 - 1 \text{ g cm}^{-2}$, in a roughly spherical envelope at $\Sigma \approx 0.025 - 0.25 \text{ g cm}^{-2}$ are quite similar to the numerical simulations by Bate et al. (2003) and Bonnell et al. (2003). In particular, the initial conditions of Bate et al. (2003) with a $M = 50 M_{\odot}$, $R = 0.19$ pc clump are closest to the properties of AFGL961. In these simulations, the clump collapses on the free-fall timescale, fragments, and produces stars in two short bursts of about 0.02 Myr duration spread by about 0.2 Myr.

The addition of radiative feedback (Bate 2009) does not change these numbers significantly.

Kurosawa et al. (2004) calculated the radiative transfer for the Bate et al. (2003) simulation and showed that the infrared classification of young stellar objects varied from Class 0 to III. Under this scenario, a protostar’s evolutionary state is dependent more on its dynamical history than its age and we would interpret the lack of circumstellar material around AFGL961B,C as due to their ejection from the dense star forming filament.

Evans et al. (2009) shows that circumstellar material around isolated low mass stars in nearby star forming regions is lost in about 0.5 Myr. If the same timescale applies to the more luminous sources in the crowded environs of AFGL961, then sources B and C are older than the cluster free-fall time suggesting a quasi-equilibrium collapse. In this scenario, evolution correlates with age and we would infer that the massive star AFGL961A formed after B and C, and that collapse continued even around this compact HII region to form dense cores SMA 2 and 3.

These observations alone cannot distinguish between dynamic or equilibrium models of cluster formation. However, similar high resolution mid-infrared through millimeter observations of other young clusters of varied luminosity and protostellar density will add to the classification statistics. In this way, we might hope to decipher the relative effect of environment and time on protostellar evolution.

5. Conclusions

We have carried out a high resolution mid-infrared and millimeter study of the central region of the young stellar cluster AFGL961. Our observations show the most deeply embedded bright protostars in the cluster and the filamentary distribution of the highest column density gas. We find five sources within 0.2 pc of each other, each with distinct properties unlike the others. The brightest infrared source is an early B star that powers a compact HII region and lies within a dense molecular core. The core mass is a substantial fraction of the stellar mass indicative of a Class I protostar. The two other infrared sources are not detected at millimeter wavelengths and the ratio of circumstellar to stellar mass is very low, suggesting that these sources are most similar to Class II objects. Further, one has cleared out a cavity in the circumcluster envelope. The SMA data also reveal two millimeter cores with no infrared counterparts. One is a strong source of line emission, drives an outflow, and has the characteristics of a deeply embedded Class 0 protostar. The other core is massive, starless, and appears to be collapsing.

The dense mixture of diverse protostellar evolutionary states suggests either that circumstellar matter is removed rapidly through dynamical interactions with other cluster members

or that clusters build up gradually over several free-fall timescales. Regardless of its history, however, the discovery of a massive, collapsing core shows that AFGL961 continues to grow even after the birth of a massive star.

J.P.W. acknowledges the NSF for support through grants AST-0324328 and AST-0607710 and BHO for his support of the NSF. We thank Matthew Bate and Ian Bonnell for comments. This publication makes use of data products from the Two Micron All Sky Survey, which is a joint project of the University of Massachusetts and the Infrared Processing and Analysis Center/California Institute of Technology, funded by the National Aeronautics and Space Administration and the National Science Foundation, and the facilities of the Canadian Astronomy Data Centre operated by the National Research Council of Canada with the support of the Canadian Space Agency.

REFERENCES

- Andre, P., Ward-Thompson, D., & Barsony, M. 1993, *ApJ*, 406, 122
- Aspin, C. 1998, *A&A*, 335, 1040
- Bally, J., & Predmore, R. 1983, *ApJ*, 265, 778
- Bate, M. R., Bonnell, I. A., & Bromm, V. 2003, *MNRAS*, 339, 577
- Bate, M. R. 2009, *MNRAS*, 392, 1363
- Bertoldi, F., & McKee, C. F. 1992, *ApJ*, 395, 140
- Blitz, L., & Thaddeus, P. 1980, *ApJ*, 241, 676
- Bonnell, I. A., Bate, M. R., & Vine, S. G. 2003, *MNRAS*, 343, 413
- Castelaz, M. W., Grasdalen, G. L., Hackwell, J. A., Capps, R. W., & Thompson, D. 1985, *AJ*, 90, 1113
- Cohen, M. 1973, *ApJ*, 185, L75
- Cox, P., Deharveng, L., & Leene, A. 1990, *A&A*, 230, 181
- Dent, W. R. F., et al. 2009, arXiv:0902.4138
- De Vries, C. H., & Myers, P. C. 2005, *ApJ*, 620, 800

- de Wit, W. J., et al. 2009, *A&A*, 494, 157
- Evans, N. J., et al. 2009, *ApJS*, 181, 321
- Hildebrand, R. H. 1983, *QJRAS*, 24, 267
- Hensberge, H., Pavlovski, K., & Verschueren, W. 2000, *A&A*, 358, 553
- Hunter, T. R., Brogan, C. L., Megeath, S. T., Menten, K. M., Beuther, H., & Thorwirth, S. 2006, *ApJ*, 649, 888
- Jørgensen, J. K., et al. 2006, *ApJ*, 645, 1246
- Kassis, M., Adams, J. D., Hora, J. L., Deutsch, L. K., & Tollestrup, E. V. 2008, *PASP*, 120, 1271
- Kurosawa, R., Harries, T. J., Bate, M. R., & Symington, N. H. 2004, *MNRAS*, 351, 1134
- Lada, C. J., & Gautier, T. N., III 1982, *ApJ*, 261, 161
- Lenzen, R., Hodapp, K.-W., & Reddmann, T. 1984, *A&A*, 137, 365
- Li, J. Z., Smith, M. D., Gredel, R., Davis, C. J., & Rector, T. A. 2008, *ApJ*, 679, L101
- Mardones, D., Myers, P. C., Tafalla, M., Wilner, D. J., Bachiller, R., & Garay, G. 1997, *ApJ*, 489, 719
- Ogura, K., & Ishida, K. 1981, *PASJ*, 33, 149
- Perez, M. R., The, P. S., & Westerlund, B. E. 1987, *PASP*, 99, 1050
- Poulton, C. J., Robitaille, T. P., Greaves, J. S., Bonnell, I. A., Williams, J. P., & Heyer, M. H. 2008, *MNRAS*, 384, 1249
- Robitaille, T. P., Whitney, B. A., Indebetouw, R., Wood, K., & Denzmore, P. 2006, *ApJS*, 167, 256
- Robitaille, T. P., Whitney, B. A., Indebetouw, R., & Wood, K. 2007, *ApJS*, 169, 328
- Rodón, J. A., Beuther, H., Megeath, S. T., & van der Tak, F. F. S. 2008, *A&A*, 490, 213
- Román-Zúñiga, C. G., Elston, R., Ferreira, B., & Lada, E. A. 2008, *ApJ*, 672, 861
- Shepherd, D. S., Kurtz, S. E., & Testi, L. 2004, *ApJ*, 601, 952
- Shirley, Y. L., Evans, N. J., II, Rawlings, J. M. C., & Gregersen, E. M. 2000, *ApJS*, 131, 249

- Siess, L., Dufour, E., & Forestini, M. 2000, *A&A*, 358, 593
- Stark, R., van der Tak, F. F. S., & van Dishoeck, E. F. 1999, *ApJ*, 521, L67
- Stanimirovic, S. 2002, *Single-Dish Radio Astronomy: Techniques and Applications*, 278, 375
- Swift, J. J., & Welch, W. J. 2008, *ApJS*, 174, 202
- Tan, J. C., Krumholz, M. R., & McKee, C. F. 2006, *ApJ*, 641, L121
- Tieftrunk, A. R., Gaume, R. A., Claussen, M. J., Wilson, T. L., & Johnston, K. J. 1997, *A&A*, 318, 931
- Williams, J. P., Blitz, L., & Stark, A. A. 1995, *ApJ*, 451, 252
- Williams, J. P., & Myers, P. C. 1999, *ApJ*, 518, L37
- Zinnecker, H., & Yorke, H. W. 2007, *ARA&A*, 45, 481

Table 1. Infrared sources

Source	$\Delta\alpha^a$ (")	$\Delta\delta^a$ (")	J (Jy)	H (Jy)	K (Jy)	M (Jy)	N (Jy)	Q (Jy)
AFGL961A	0.0	0.0	0.006	0.023	0.009	18.7	37.2	159
AFGL961B	−4.9	−1.7	0.026	0.147	0.029	3.98	12.3	74.0
AFGL961C	−30.8	1.3	0.539	0.598	0.085	0.55	2.05	17.0

$$^a\alpha_{2000} = 06^{\text{h}}34^{\text{m}}37.74^{\text{s}}, \delta_{2000} = 04^{\circ}12'44.2''$$

Table 2. Millimeter cores

Source	$\Delta\alpha$ (")	$\Delta\delta$ (")	S_{1400} (mJy)	M_{core}^a (M_{\odot})	$v_{\text{l sr}}$ (km s^{-1})	Δv (km s^{-1})	M_{vir}^b (M_{\odot})
SMA1	0.2	0.0	215	6.3	15.0	2.1	13
SMA2	−5.0	−0.1	184	5.4	14.2	4.3	56
SMA3	−16.8	4.0	210	6.2	12.6	1.8	9.8

$$^aT = 20 \text{ K}, \kappa_{\nu} = 0.19 \text{ cm}^2 \text{ g}^{-1}$$

$$^bR = 5000 \text{ AU}$$

Table 3. SED fits

Source	M_{*} (M_{\odot})		L (L_{\odot})	
	Best	Mean	Best	Mean
AFGL961A	11.0	11.3 ± 1.8	4600	6000 ± 2500
AFGL961B	9.1	9.1 ± 1.3	1200	2500 ± 1300
AFGL961C	5.3	6.4 ± 1.1	370	480 ± 200

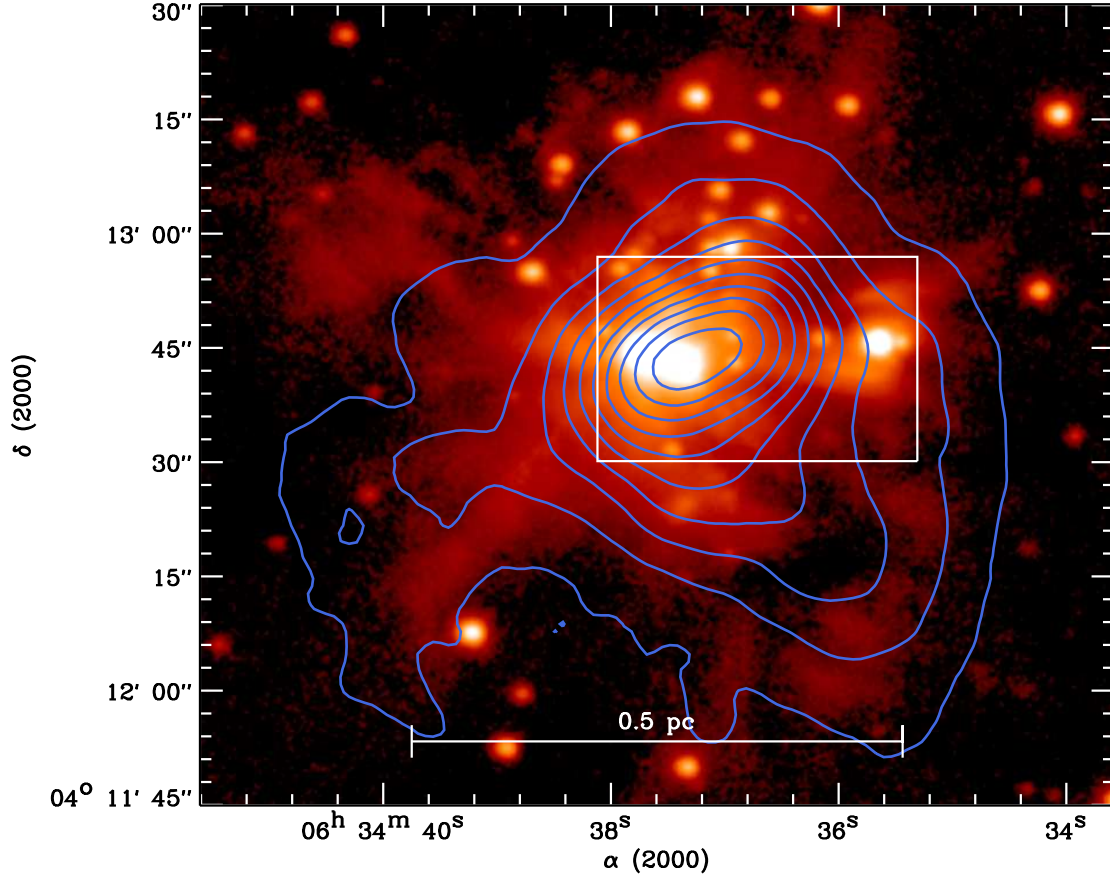


Fig. 1.— Large scale view of the AFGL961 cluster. The background is the K-band image from Román-Zúñiga et al. (2008) on a log scale showing the embedded stars and associated nebulosity. The contours of the SCUBA 850 μm emission from the cold, dusty cluster envelope show surface densities at $\Sigma = 0.025 \times (1, 2, 3\dots) \text{ g cm}^{-2}$. The rectangle outlines the region shown in the MIRSI images in Figure 2.

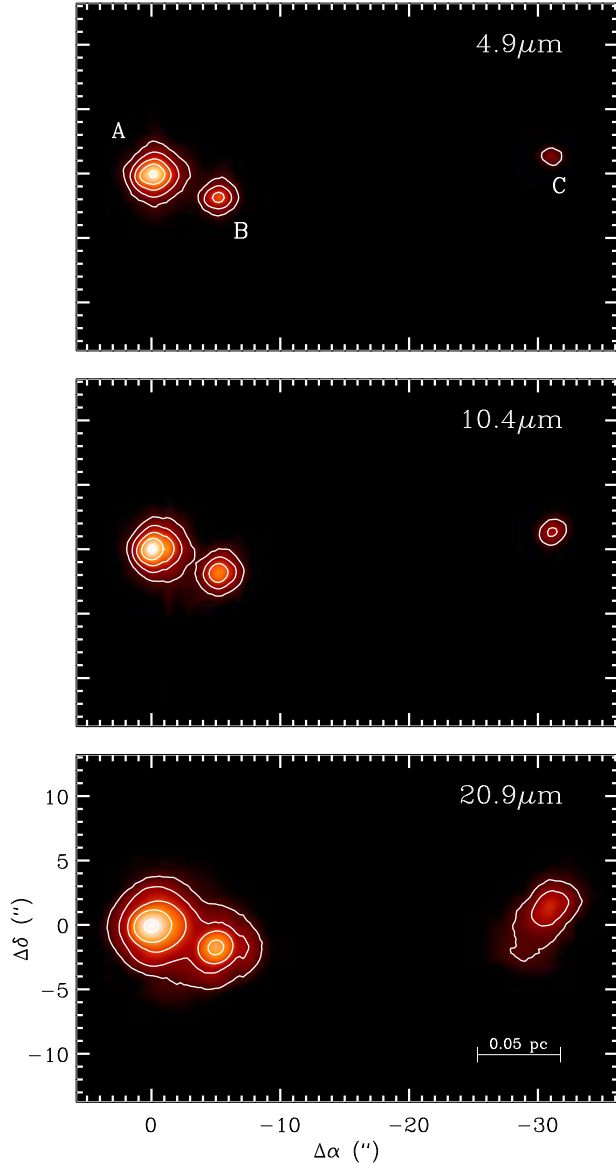


Fig. 2.— MIRSI maps of the center of AFGL961 at M, N, and Q bands (4.9 , 10.4 , and $20.9\mu\text{m}$ respectively). For each band, the scale is logarithmic with a dynamic range of 300 and the contour levels are at 1, 3, 9, 27, 81% of the peak intensity. The axes are arcsecond offsets from AFGL961A.

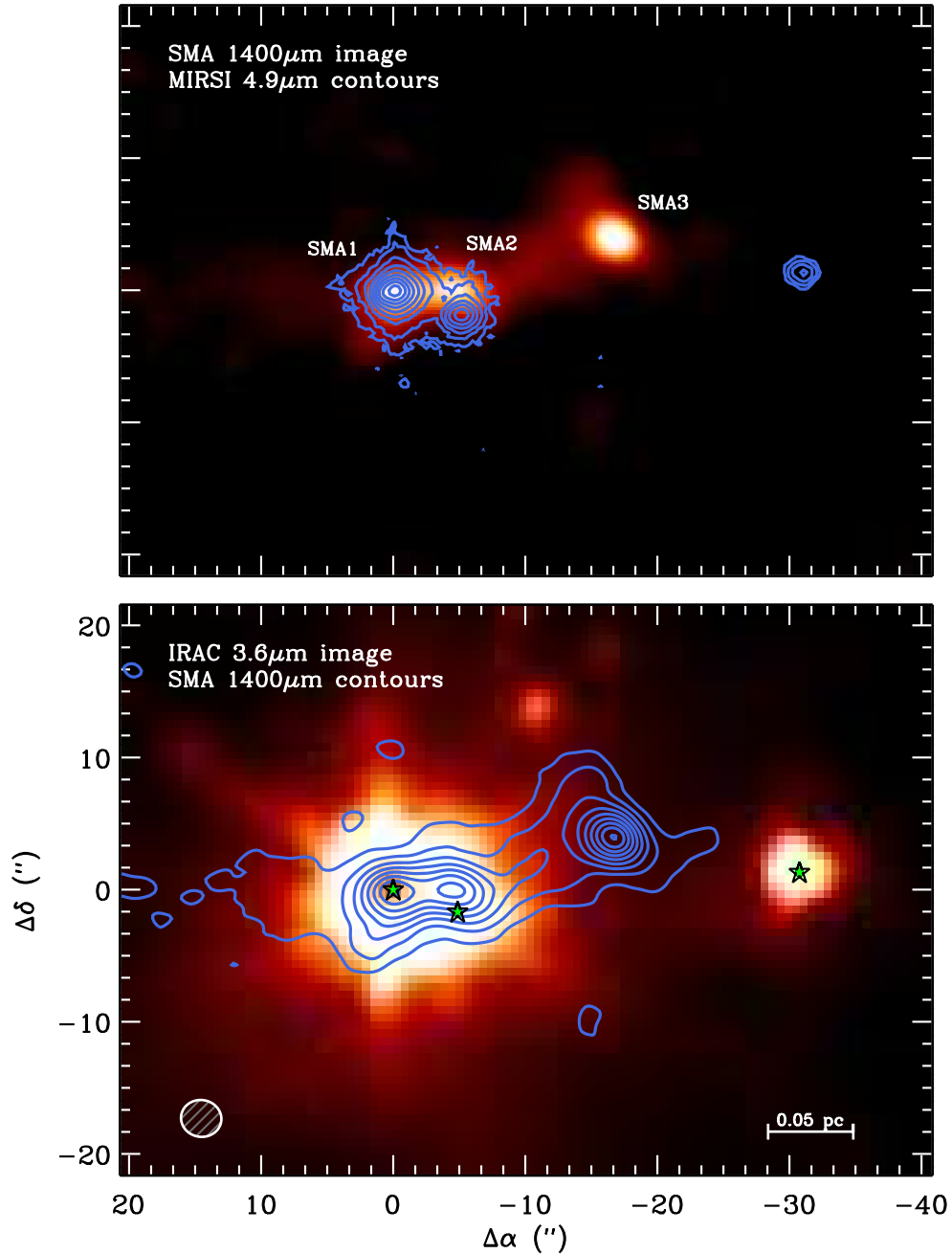


Fig. 3.— The 1400 μm continuum emission from the SMA data showing the cool dust condensations in the cluster. The top panel overlays the MIRSI M-band image in logarithmic contours on the 1400 μm continuum map. The scale ranges linearly from 5 to 75 mJy beam^{-1} , corresponding to surface densities $\Sigma = 0.05$ to 0.75 g cm^{-2} . The three prominent millimeter peaks are labeled SMA1–3 and their properties listed in Table 2. The bottom panel overlays the 1400 μm continuum map in contours on the Spitzer 3.6 μm map in log scale. The contours are at surface densities $\Sigma = 0.1 \times (1, 2, 3\dots) \text{ g cm}^{-2}$. The stars show the locations of the MIRSI sources AFGL961A,B,C. The Spitzer image is saturated at the positions of these sources but provides stringent limits on the luminosity of any embedded source in SMA3. The $3''.1 \times 2''.8$ SMA beam is shown in the lower left corner.

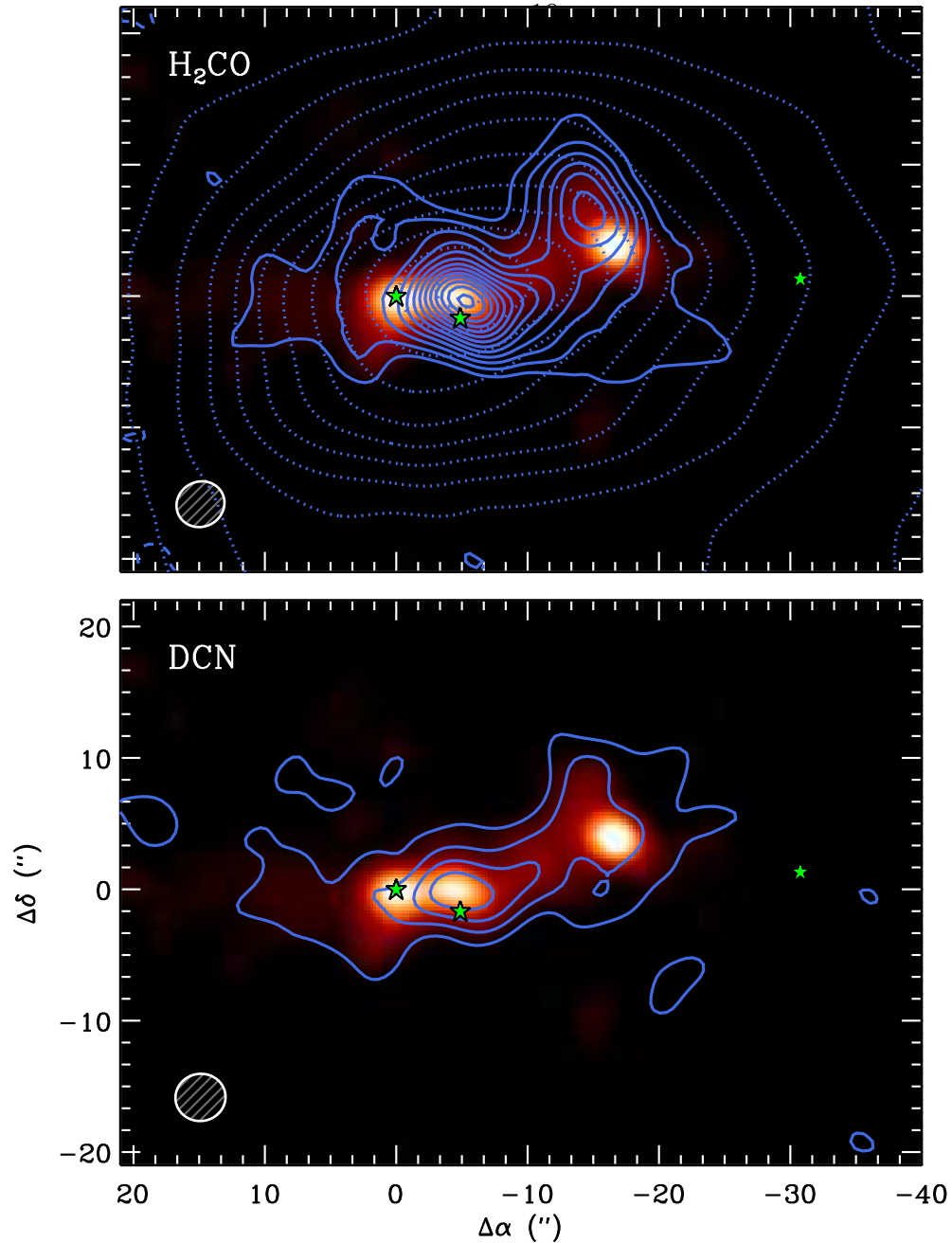


Fig. 4.— Integrated intensity maps of H_2CO $3_{12} - 2_{11}$ (top panel) and DCN $3 - 2$ (bottom panel). The background image in each case is the $1400\ \mu\text{m}$ continuum map. The velocity range of integration was 8 to $20\ \text{km s}^{-1}$. For the H_2CO map, the SMA data are shown in solid contours beginning at and in increments of $0.4\ \text{K km s}^{-1}$. Dashed contours show negative levels. The combined JCMT+SMA map is shown in dotted contours at $4\ \text{K km s}^{-1}$. The DCN contours are at $0.2\ \text{K km s}^{-1}$. The stars shows the location of AFGL961A,B, and C. The resolution of the integrated intensity maps is shown in the lower left corner of each panel.

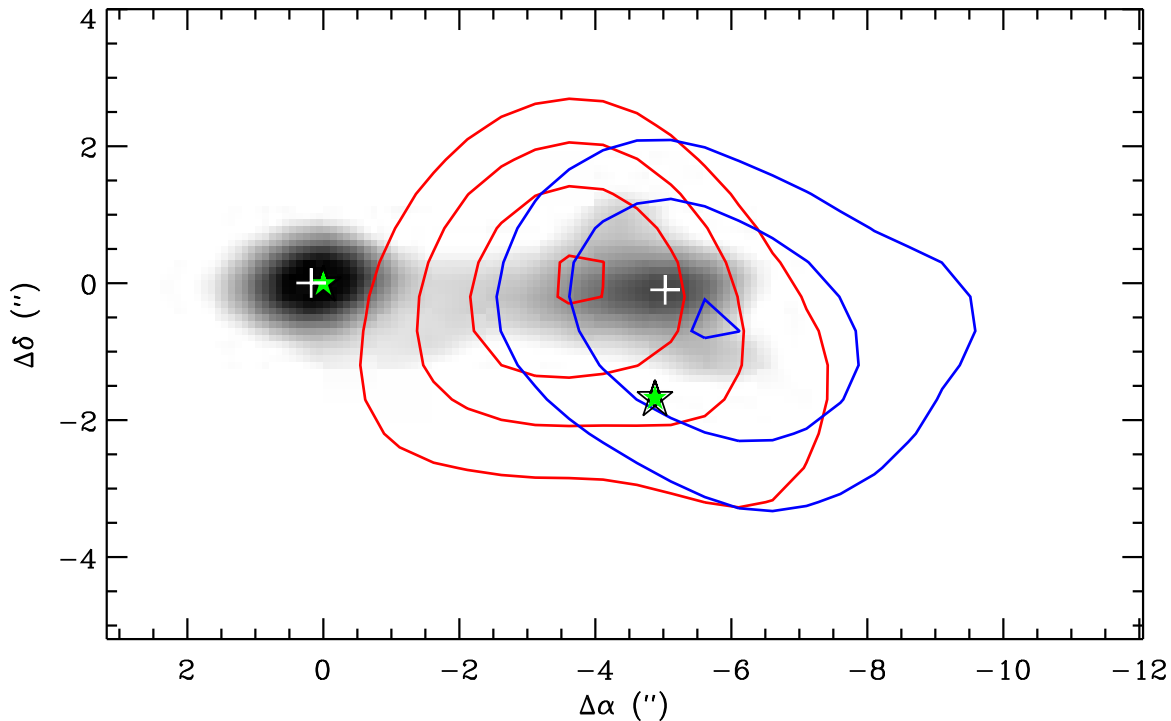


Fig. 5.— Red and blueshifted H_2CO emission revealing a molecular outflow from an (undetected) embedded protostar in SMA2. The background image is the high resolution ($1''.4 \times 0''.9$) $1400\ \mu\text{m}$ continuum map and ranges from 15 to $30\ \text{mJy beam}^{-1}$. The solid or red contours show the intensity integrated over $13 - 25\ \text{km s}^{-1}$, and the dashed or blue contours show the intensity integrated over $0 - 13\ \text{km s}^{-1}$. Contour levels are 30, 40, 50, ... K km s^{-1} , and show only the most intense emission above the cloud background. The stars show the location of AFGL961A, B and the crosses locate the peak of the millimeter cores SMA1, 2.

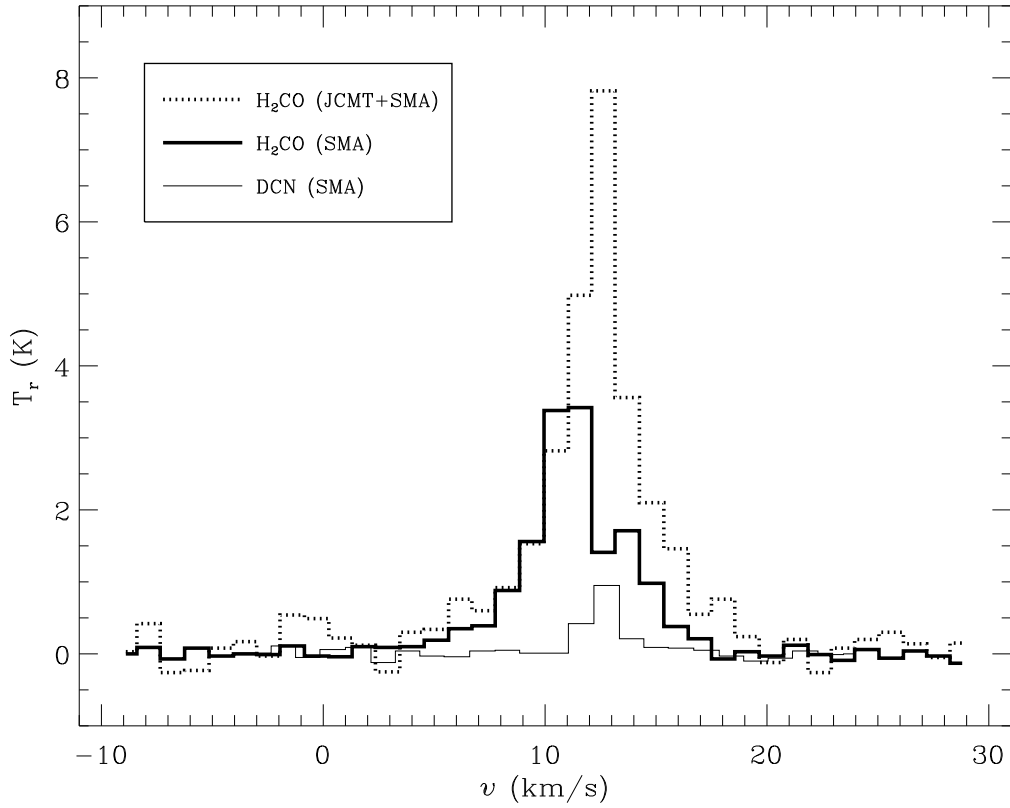


Fig. 6.— Spectra toward SMA3 showing infall at small scales, possibly due to core collapse. The thick solid line is the SMA H₂CO spectrum and shows a slight dip at the same velocity as the peak of the DCN spectrum shown as a thin solid line. The dotted line is the combined JCMT+SMA H₂CO spectrum which is more symmetric and does not show any self-absorption features.

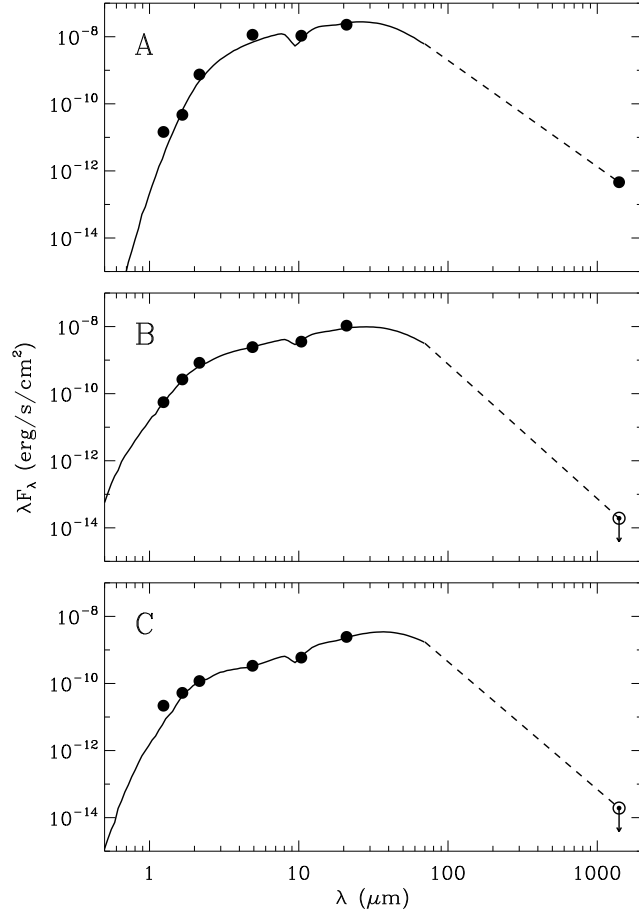


Fig. 7.— Spectral energy distributions and best fit model for the three infrared sources AFGL961A,B,C. The dotted line linearly interpolates between the model at $70 \mu\text{m}$ and SMA data point at $1400 \mu\text{m}$.